Supporting information

Commercial-Level Mass-Loading MnO$_2$ with Ion Diffusion Channels for High-Performing Aqueous Energy Storage Devices

Yaxiong Zhang[a]‡, Xiaosha Cui[a]‡, Jiecai Fu[a, *], Yupeng Liu[a], Yin Wu[a], Jinyuan Zhou[a], Zhenxing Zhang[a], Erqing Xie[a, *]

[a]Key Laboratory for Magnetism and Magnetic Materials of the Ministry of Education, School of Physical Science and Technology, Lanzhou University, Lanzhou 730000, China

‡ These authors contributed equally to this work.

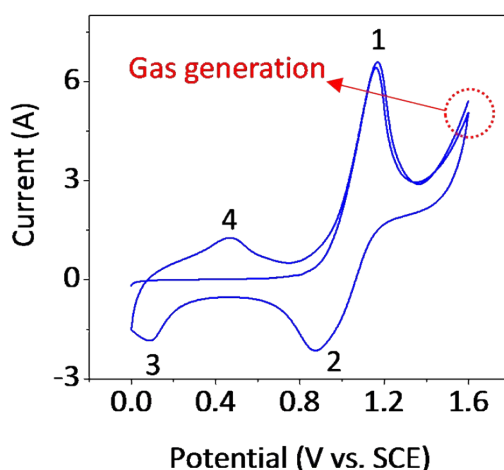*Corresponding authors, E-mail: fujc@lzu.edu.cn (J. Fu); xieeq@lzu.edu.cn (E. Xie)

Figure S1. First and half-second cycles of CV electrodeposition with four special peaks.

During the initial CV curve of electrodeposition, three distinct peaks were observed. The first was numbered as "1" and the two others as "2" and "3". In the first cycle, the significant polarization at 1.6 V led to electrolysis of water accompanied by the production of gas bubbles. The fourth peak numbered as "4" in the charging curve occurred during the second cycle. Note that there is no oxidation peak of Mn^{2+}/Mn^{3+} at the position of "4" for the first cycle, which occurs in the second cycle. It can be

explained that rare Mn^{3+} ions can be formed in the initial deposition electrolyte due to the acid conditions (with the pH value of 2.85) but not for the Mn^{4+} ions, which is also reported in the previous reports (*Hydrometallurgy* **2016**, *166*, 279-284). After the charging operations at the end of first cycle, the intercalation of proton in the MnO_2 formed in the first cycle results the change of acidity for the deposition electrolyte in the second cycle, which makes it possible for the oxidation process of $Mn^{2+}=>$ Mn^{3+} (*i.e.,* the oxidation peak "4" occurs in the second cycle).
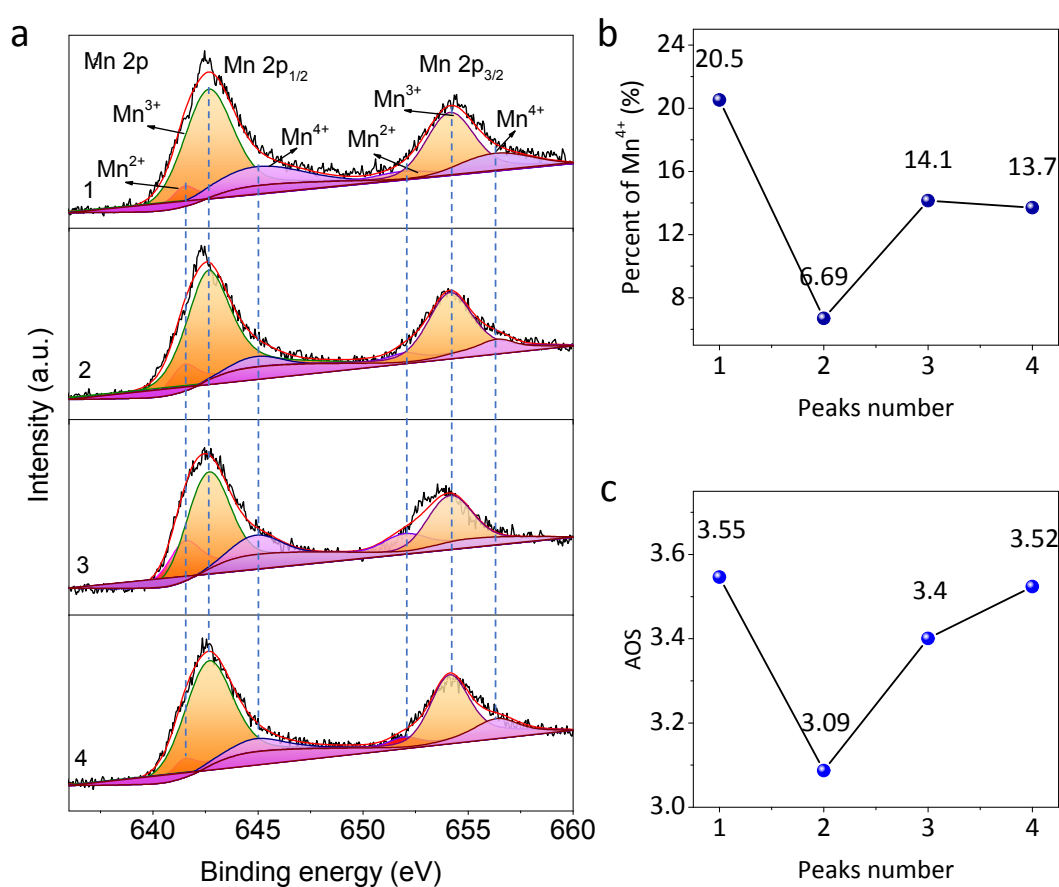

Figure S2. (a) Fine XPS spectra of Mn 2p, (b) percent of Mn^{4+}, (c) and AOS of the four peaks.

The Mn $2p_{2/3}$ spectrum exhibited three fitted peaks at 641.5, 642.6 and 645.1 eV, belonging to Mn^{2+}, $Mn^{3+,}$ and Mn^{4+}, respectively. The variation in Mn^{4+} content in Figure S2b showed the highest value at Peak 1 in the CV curve. This implied the formation of birnessite-MnO_2, consistent with the Raman

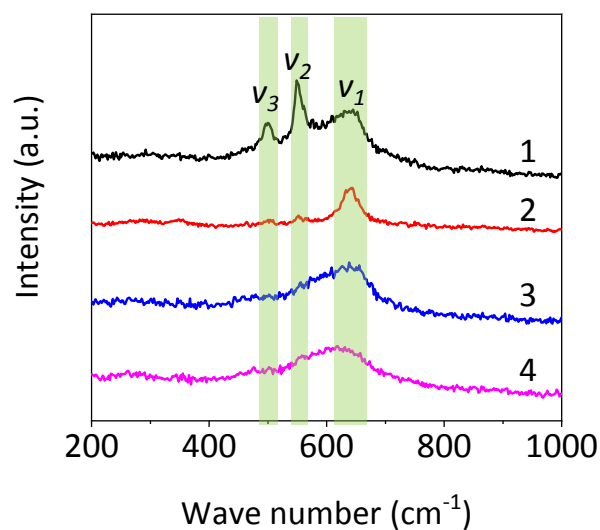results. The same conclusions can be obtained from Figure S2c using the AOS.

Figure S3. Raman spectra of the four peaks.

The Raman spectrum at Peak 1 showed the birnessite-MnO_2 characteristic with three significant features: v_1 at 625~650 cm^{-1}, v_2 at 575~585 cm^{-1}, and v_3 at 480~505 cm^{-1}. Thus, oxidation took place at this time and birnessite-MnO_2 formed on the carbon fiber surface. In principle, v_1 and v_2 would define the signals of lattice force due to Na^+ ions adsorption on the layer surface, and v_3 represented the signal of Na^+ ions intercalated in the layer combined with influence the layer spacing. In subsequent discharge processes (reduction reaction), the intensity of the Raman characteristic peak v_1 at Peak 2 in CV curve gradually increased, meaning the adsorption of large amounts of Na^+ ions on the electrode surface. The same situation was also reflected at CV Peak 3. For Peak 4, the Raman features of birnessite-MnO_2 became progressively less pronounced due to laminar aberrations or disordered structure of the electrode surface.
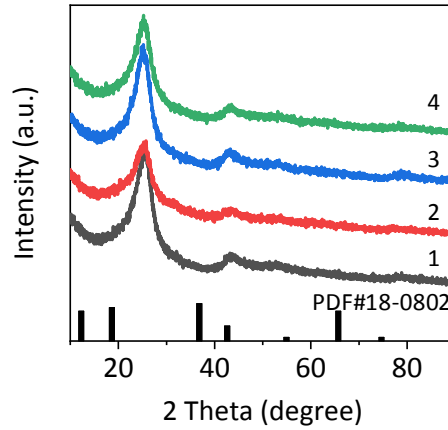
Figure S4. XRD of the four peaks in CV electrodeposition curves.

The initial cycle of CV electrodeposition showed very poor XRD signal due to the clutter of the crystallography and low loading amounts.
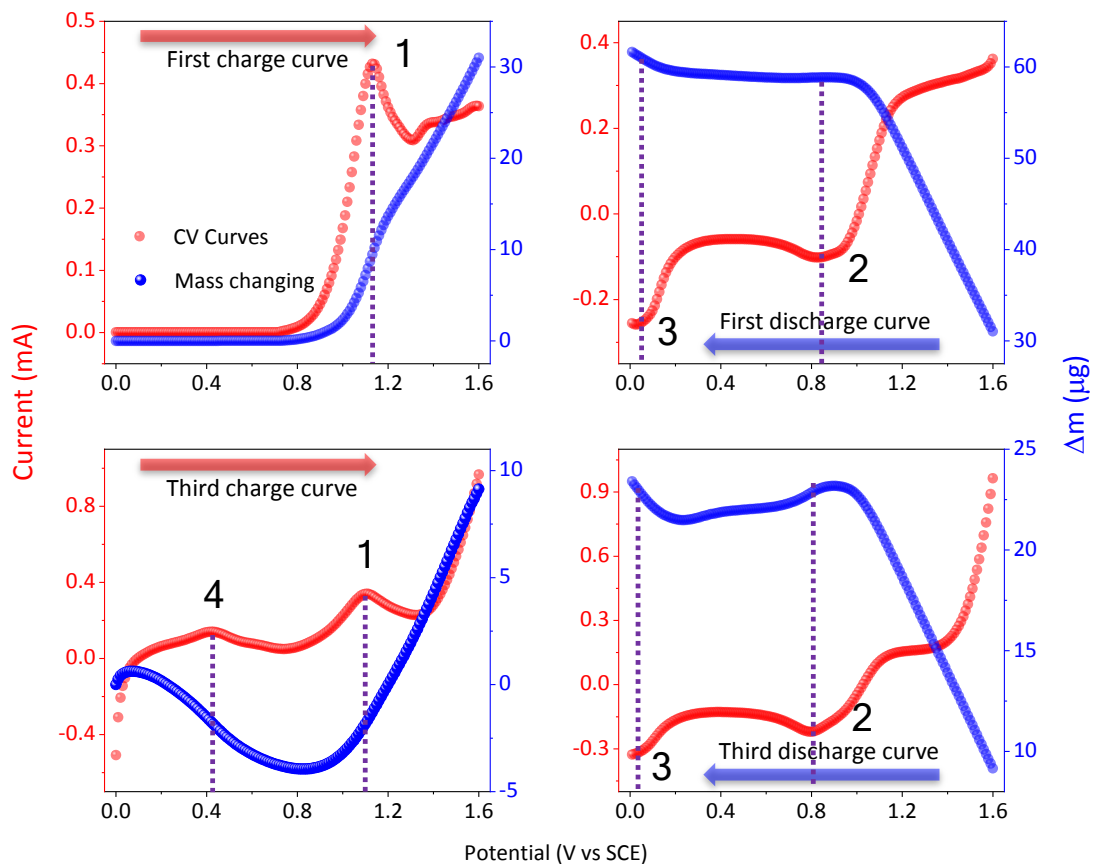

Figure S5. Electrochemical quartz crystal microbalance (EQCM) analyses and corresponding charge/discharge CV curves at the scan rate of 5 mV/s for the first and third cycles.

To better quantify the CV electrodeposition, *in-situ* EQCM was conducted to track the behaviors of

Na$^+$ ions and Mn. Since EQCM was highly sensitive to changes in mass, the adsorption and desorption signals of Mn^{2+} and Na$^+$ can be provided along with the insertion/de-insertion process of Na$^+$. The relationship between the resonance frequency shift and mass variation of the EQCM sensor can be described by the Sauerbrey equation (Eq. (1)):

$$\Delta m = -\frac{A\sqrt{\mu \cdot \rho}}{2f_0^2} \cdot \Delta f = - C_f \cdot \Delta f \tag{1}$$

where Δf is the frequency shift in the EQCM sensor (Au-masked quartz crystal-based electrode in experimental), f_0 (7.995 MHz) represents the fundamental resonance frequency of the EQCM sensor, Δm denotes the mass variation, A refers to the area of the active surface of the electrode (0.196 cm^2), μ is the shear factor (2.947*10^{11} g/cm·s^2), and ρ corresponds to the density of quartz crystal (2.684 g/cm^3). Note that an inherent factor C_f of 1.36 ng/Hz·cm^2 was obtained.

During the first charging process, an increasing trend of mass was noticed after a stable mass change at Peak "1". Such a process can be attributed to the deposition of Mn^{2+} ions. During the first discharging process, the mass of the electrode still kept an increasing trend until the end of the charging process. This can be explained by the positive effect of current, causing continued removal of ions. The mass then kept stable at Peak "2", meaning the reduction in Mn (III/IV). At Peak "3", the rise in mass indicated the adsorption of Na$^+$ and insertion process of Na$^+$. During the third charging process, Peak "4" appeared along with a decline in mass, suggesting desertion process of Na$^+$. The subsequent mass change showed the same trend as the first charging-discharging process.
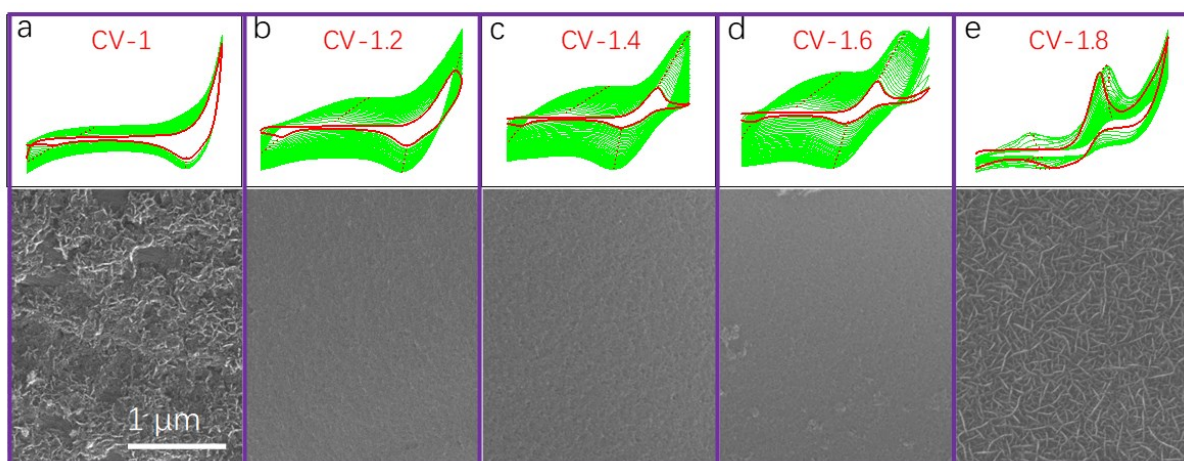
Figure S6. CV electrodeposition processes of CV-1, CV-1.2, CV-1.4, CV-1.6, and CV-1.8 along with the corresponding SEM images.
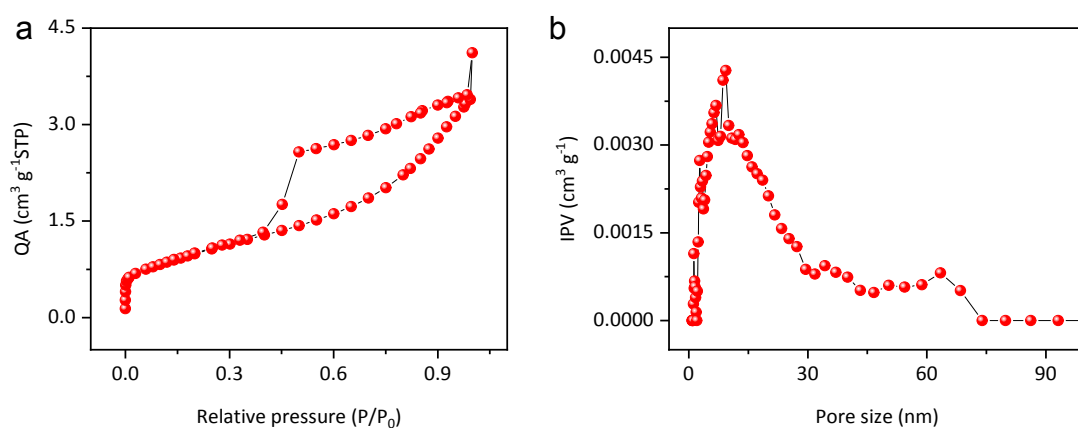

Figure S7. (a) N_2 adsorption and desorption isotherms. (b) Pore size distribution of CV-1.6 (Quantity Adsorbed (QA), Inc. Pore Volume (IPV)).
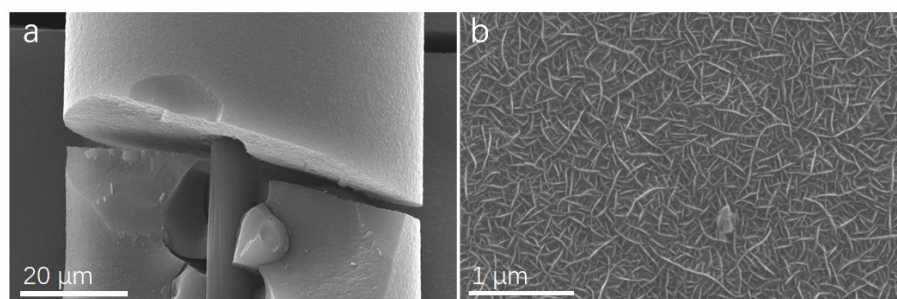

Figure S8. Typical SEM images (cross-sectional and surface) of high mass loading MnO_2 under constant current deposition.
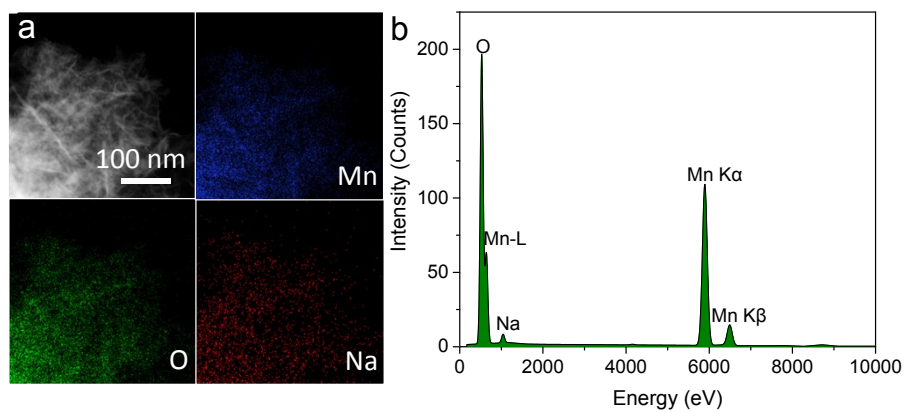
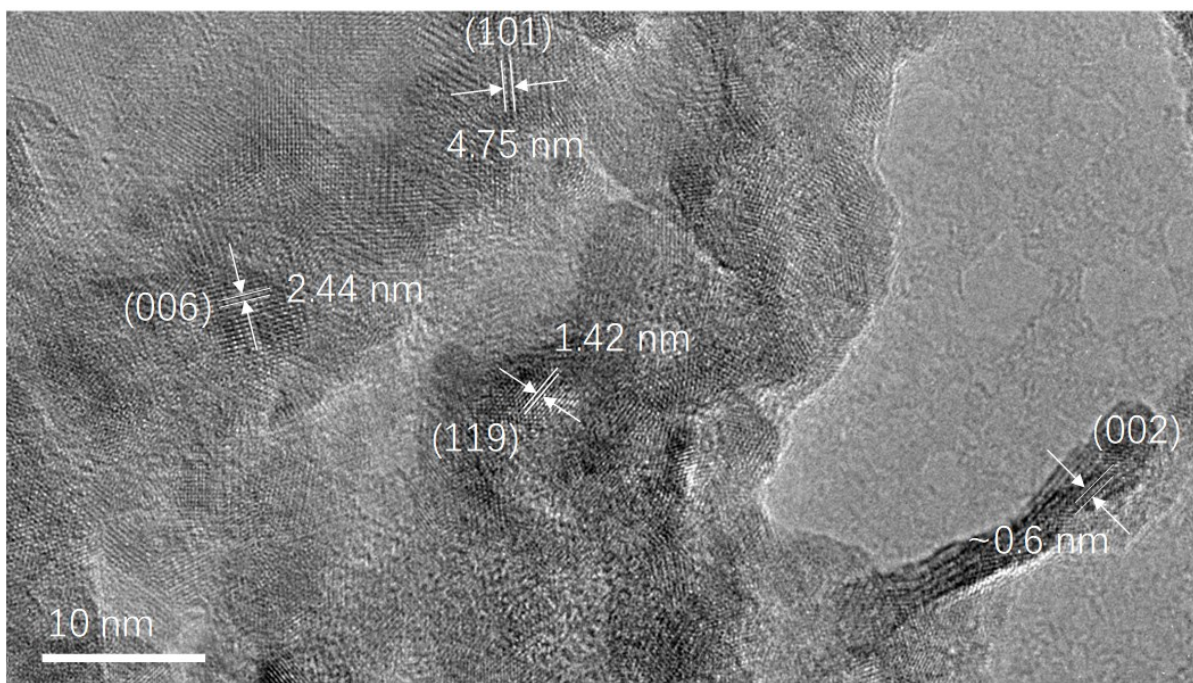**Figure S9.** EDS-mapping (a) and spectrum (b) of the sample CV-1.6.

Figure S10. HRTEM image of CV-1.6.
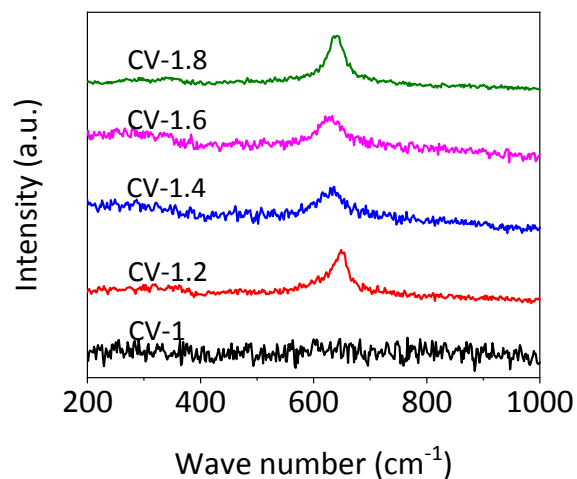
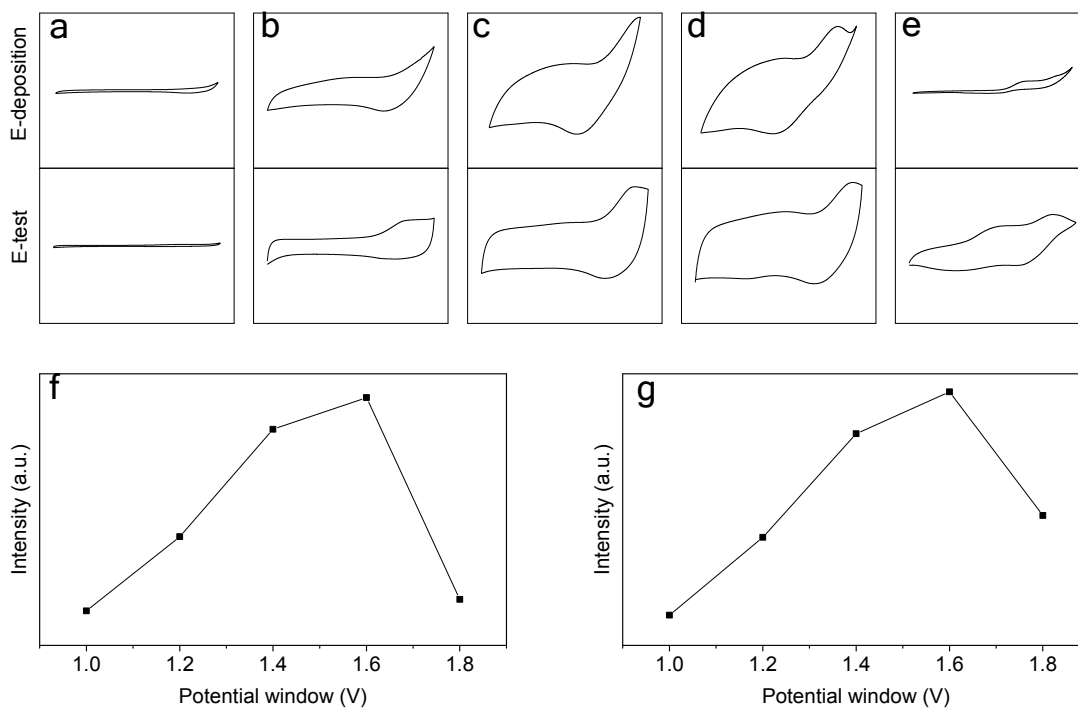**Figure S11.** Raman spectra of CV-1, CV-1.2, CV-1.4, CV-1.6, and CV-1.8.

Figure S12. (a-e) The last CV curves of the electrodeposition processes of CV-1, CV-1.2, CV-1.4, CV-1.6, and CV-1.8 are shown the corresponding electrochemical performances in CV at the scan rate of 5 mV/s. (f) Change in peak intensity of CV electrodeposition. (b) Change in peak intensity of the electrochemical performance tests under different potential windows.
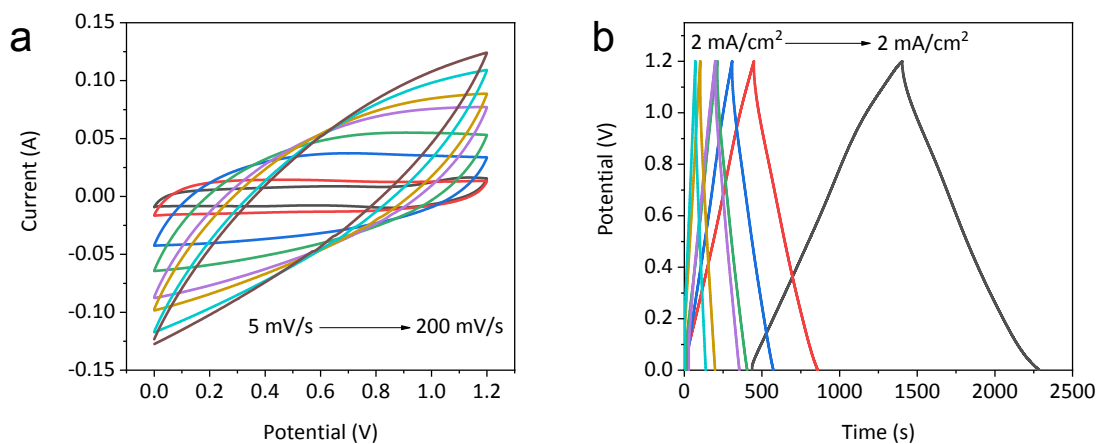
Figure S13. Na^{+} based electrolyte, CV curves at different scan rates and GCD curves at different current densities.
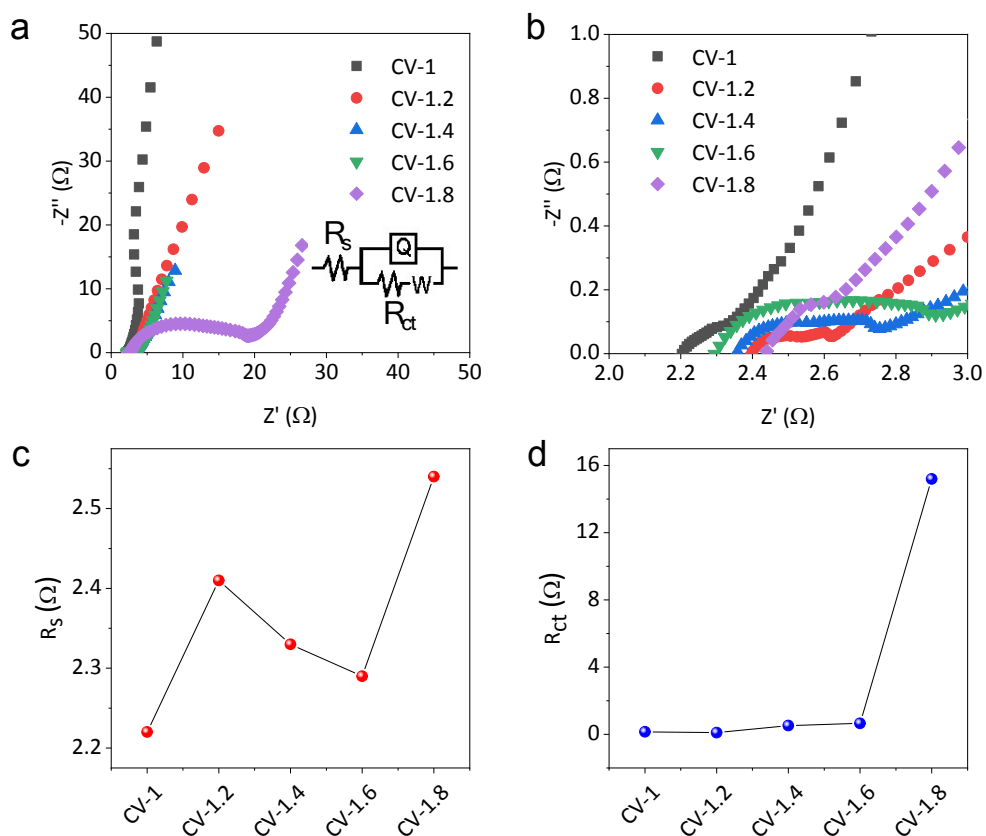

Figure S14. Na^{+} based electrolyte, (a) Nyquist plots (inset shows an equivalent circuit model); (b) High-frequency region. (c) R_s and R_{ct} of CV-1, CV-1.2, CV-1.4, CV-1.6, and CV-1.8.
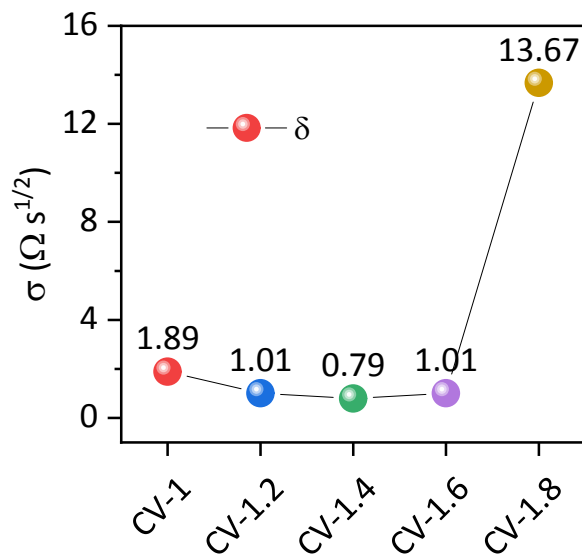
Figure S15. Na^+ based electrolyte, Warburg coefficient σ values obtained by linear fitting of Z' versus $\omega^{-1/2}$ plots in the high-frequency region for different samples.
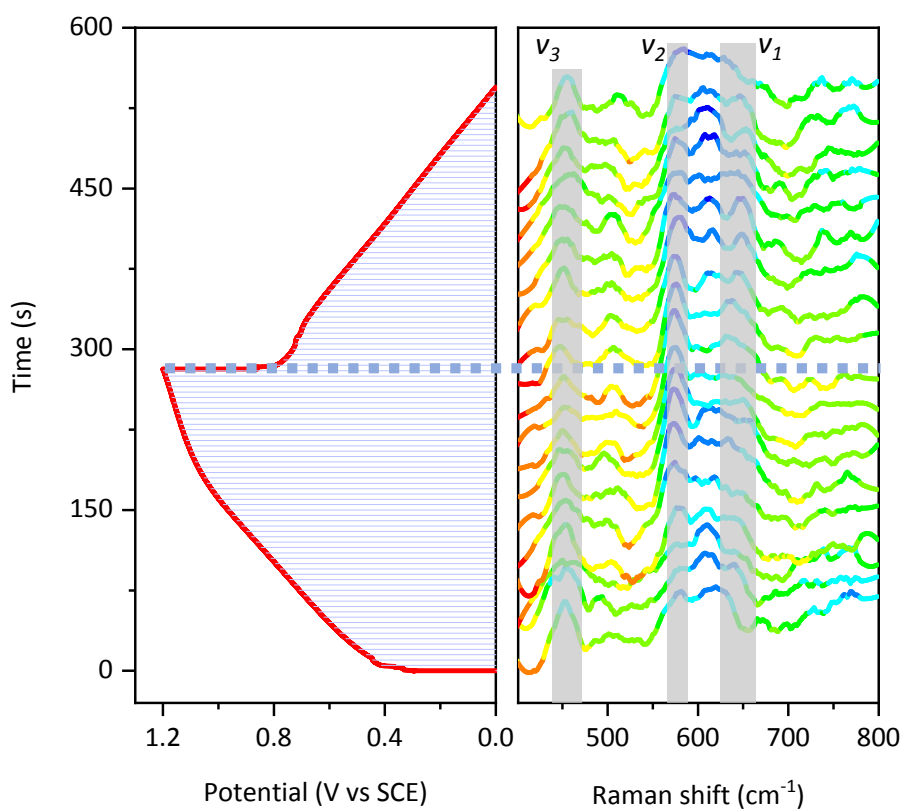

Figure S16. Na^+ based electrolyte, *in-situ* Raman analysis of GCD curves (2 mA/cm^2) under charge/discharge processes of CV-1.6.

For Raman signals of birnessite-MnO_2, v_1 and v_2 peaks corresponded to the Mn-O stretching vibration of [MnO_6] octahedra, and v_3 corresponded to the interaction between the ions and layers.
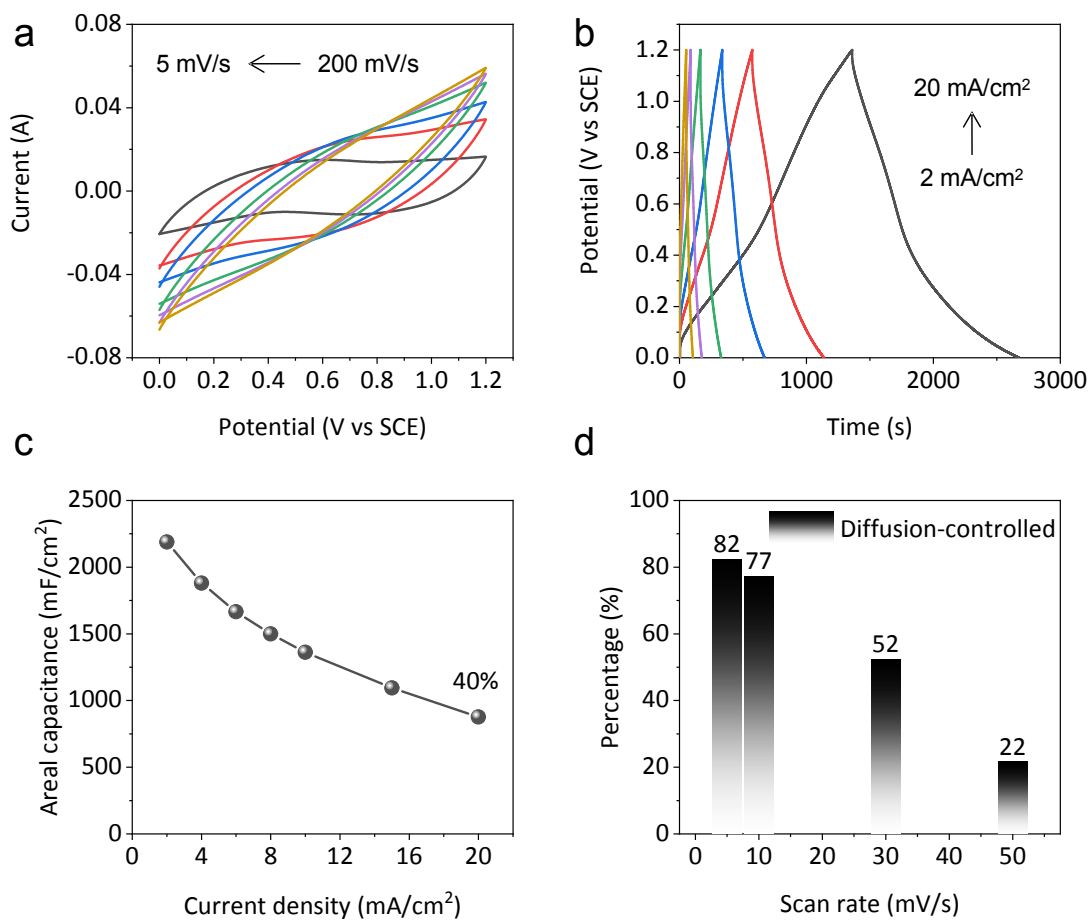

Figure S17. Mg^{2+} based electrolyte, (a) CV curves at different scan rates and (b) GCD curves at different current densities, (c) GCD derived areal capacitance values at different current densities, (d) and the calculated diffusion-controlled capacitance percentage of the total capacitance.
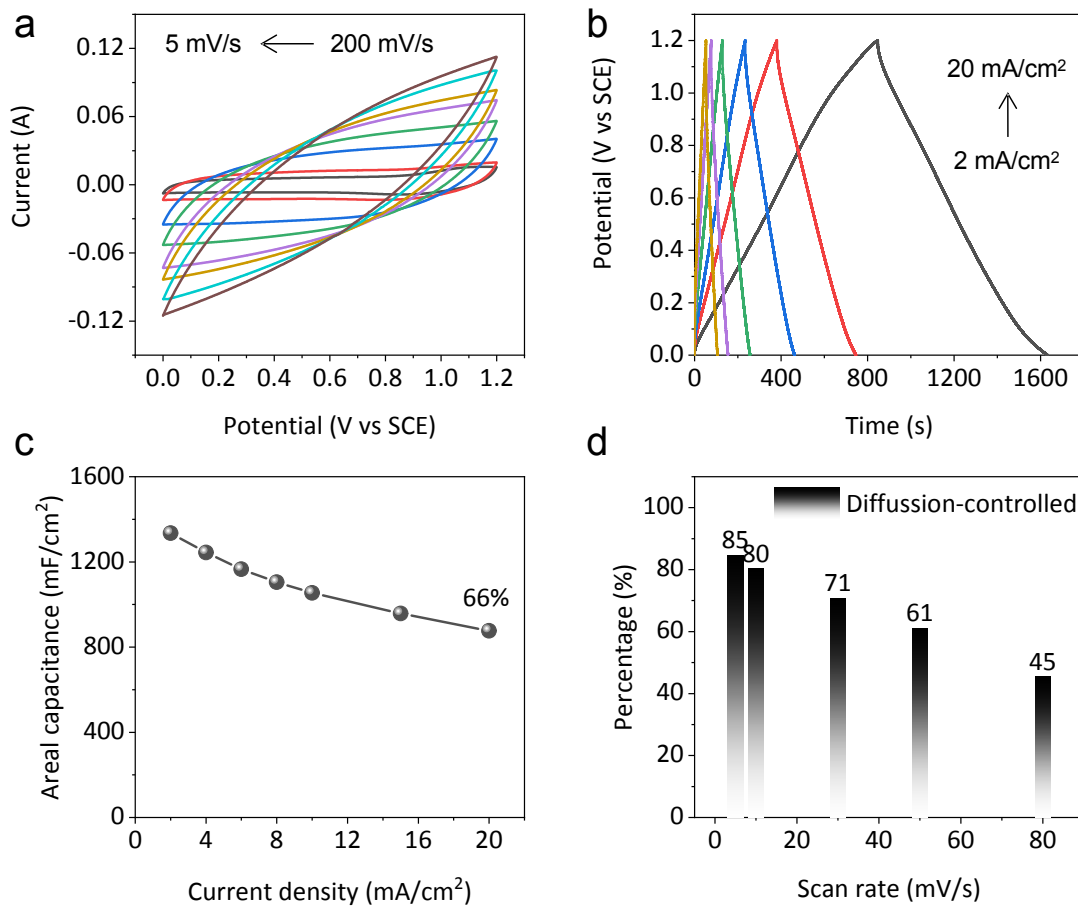
Figure S18. Zn^{2+} based electrolyte, (a) CV curves at different scan rates and (b) GCD curves at different current densities, (c) GCD derived areal capacitance values at different current densities, (d) and the calculated diffusion-controlled capacitance percentage of the total capacitance.
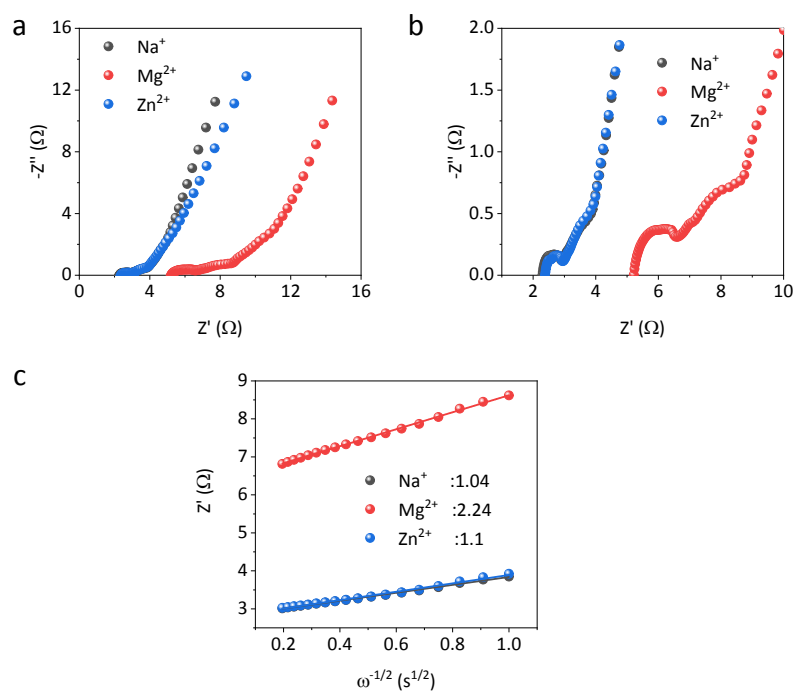
Figure S19. (a) Nyquist plots ; (b) High-frequency region. (c) Warburg coefficient σ values obtained

by linear fitting of Z' versus $\omega^{-1/2}$ plots in the high-frequency region for different electrolytes.
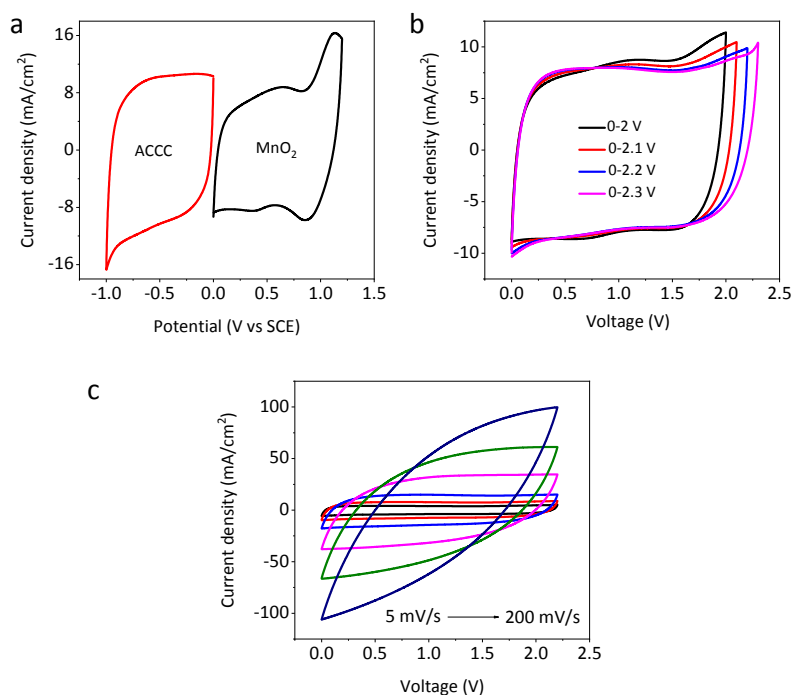

Figure S20. Na$^+$ based electrolyte, Electrochemical performances of the assembled asymmetric

supercapacitors (ACCC//MnO$_2$). (a) CV curves of the cathode and anode at the scan rate of 20 mV/s;

(b) CV curves at different voltage windows (with a scan rate of 10 mV/s); (c) CV curves at different
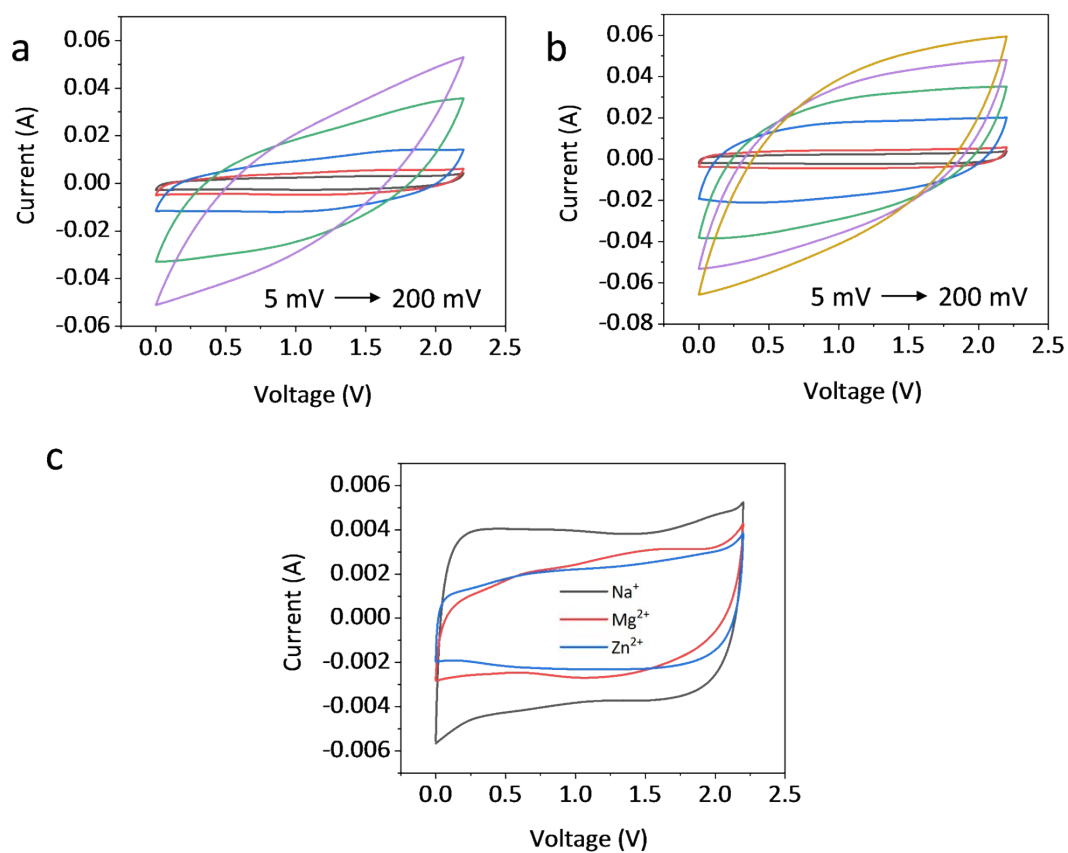
scan rates.

Figure S21. CV curves of the assembled energy storage device at different scan rates in (a) Mg^{2+} based electrolyte, (b) in Zn^{2+} based electrolyte. (c) CV curves at the scan rate of 5 mV/s in different electrolytes.
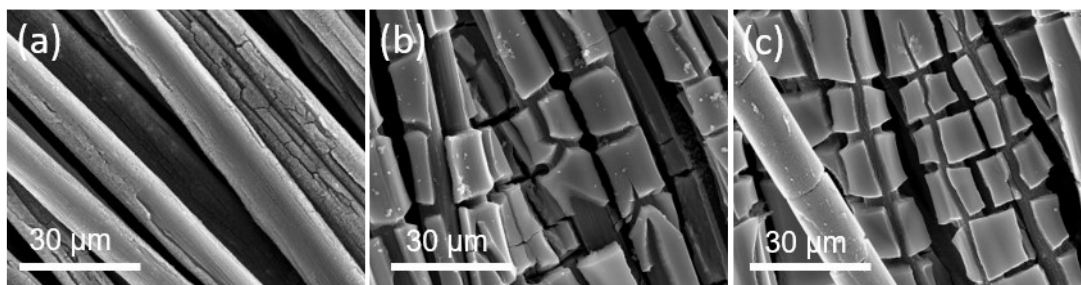

Figure S22. Morphologies of the MnO_2 electrode material cycled 10000 cycles: (a) Na^+ based electrolyte; (b) Mg^{2+} based electrolyte; (c) Zn^{2+} based electrolyte.

Figure S23. EDS-mapping results of the MnO$_2$ electrode material cycled 10000 cycles: (a) Na$^+$ based electrolyte; (b) Mg^{2+} based electrolyte; (c) Zn^{2+} based electrolyte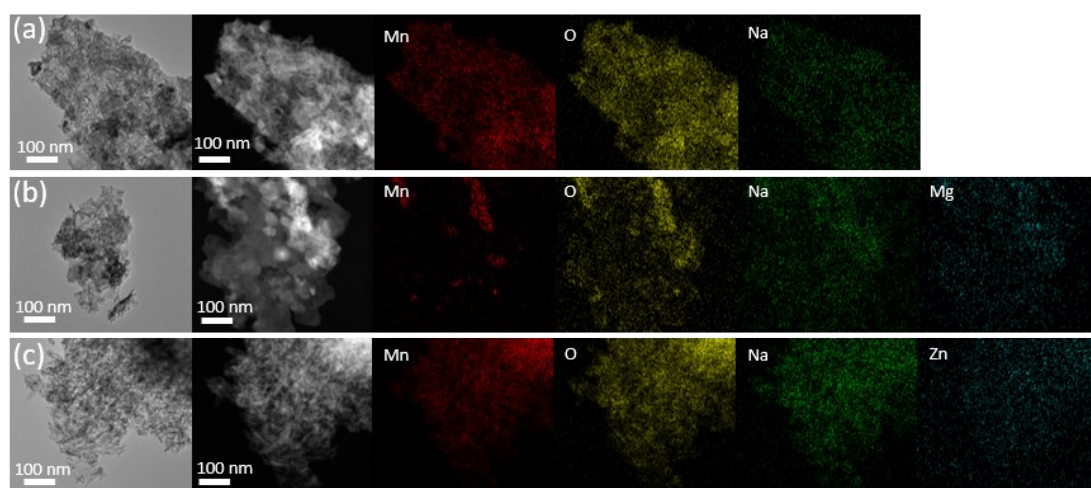.